Valle, LM.; Grima, C.; Rodríguez, R.; Llopis-Albert, C. (2020). Effect of scCO2-brine mixture on injectivity and storage capacity in rock
samples of naturally fractured carbonate formations. Journal of Natural Gas Science and Engineering. 81:1-16. https://doi.org/10.1016/j.jngse.2020.103452

Effect of $scCO_2$-brine mixture on injectivity and storage capacity in rock samples of naturally fractured carbonate formations

L. M. Valle, [1] C. Grima, [1] R. Rodríguez, [1] C. Llopis-Albert [2]

[1] Universidad Politécnica de Madrid
[2] Universitat Politècnica de València

ABSTRACT

The presence of natural fractures in the formation and its degree of heterogeneity condition the injection of CO_2 into the aquifer as they affect the migration processes and its storage capacity. In ATAP experimental facility the petrophysical behavior of two carbonate formations was studied, with different proportions of limestone, dolomite, quartz and anhydrite and fissures sealed mainly by potassium aluminosilicates and iron sulphides. Actual storage conditions (135/141 bar and 44/46 °C) corresponding to a depth of around 1500 m and continuous injection at a constant flow rate of 1cc/min of 10% and 15% of HCl, HCl/Acetic (CH_3COOH) 10%/10% and $scCO_2$ (supercritical CO_2)/brine 50%/50%, was applied to the brine saturated rock samples (coreflooding). Considering laminar flow through the fractures, the flow injected is proportional to the pressure drop according to the "cubic law" that takes into account the width and length of the fractures. This is used to evaluate the injectivity of the storage. The variations in the pressure drop are due to the dragging of detached fines in the dissolution of the carbonates of the filled fissures that can cause their opening or blocking. The efficacy of pure $scCO_2$ enriched brine injection was determined to dissolve the carbonates of the store formation compared to other methods such as the injection of acids used in the oil industry for the stimulation of producing wells. Scanning Electron Microscope (SEM) studies of the injection surfaces and Computerized Tomography (CT) analysis of the samples before and after injection of the acid mixtures have been performed. The dissolution facilitates the injectivity and increases the capacity favoring the tightness of the storage by the phenomenon of controlled dissolution-precipitation of the carbonates.

Nomenclature

A	Cross sectional area
F	Frontal
f_a	Fracture aperture
F_d	Geological formation
l	Fracture trace length
l_0	Lenght of the structural unit
II	Injectivity Index
k	Permeability
k_{CO2}	Effective CO2 permeability
k_e	Permeability under P_e
k_0	Permeability under P_0
L	Length of the plug
P	Pressure
P_e	Effective overburden pressure
P_0	Atmospheric pressure
$Pinj=P_f$	Injection pressure
P_{ob}	Overburden pressure
P_{res}	Reservoir pressure
q	Flow rate
r	Radial distance
r_e	Radius of an outer boundary
r_w	Wellbore radius
S	Skin factor
SC	Sopeña Calizo
SD	Sopeña Dolomítico
T	Temperature
v	Apparent velocity
W_s	Sample weight
X	Longitudinal
Y	Axial

Greek symbols

ΔP	Incremental pressure
ρr	Density of Injected fluid at reservoir conditions
ρs	Density of Injected fluid at standar conditions
μ	Brine/fluid viscosity
Ø	Porosity

Abbreviations

ATAP	High Temperature High Pressure
BPR	Back pressure
CT	Computerized Tomography
$scCO_2$	Supercritical CO_2
SEM	Scanning Electron Microscope
XRD	X-Ray diffraction

1. Introduction

Injectivity and capacity are two of the most important parameters that influence the technical-economic viability and safety of deep CO_2 storage (Hurtado, 2012). The development of the CO_2 sequestration process requires maintaining sustained injectivity that turns out to be little or null in the absence of effective porosity that is associated with low permeability. Understanding the processes involved in the migration of CO_2 in storages with low permeability, influenced by the natural existence of fractures and faults in the ground, allows selecting the best injection techniques that guarantee safe storage (Iding and Ringrose, 2010). The interactions that occur between CO_2-brine-rock in saline aquifers can have effects on their stability (Phuc Vu et al., 2018) and tightness, resulting more or less favorable for CO2 storage (Le Gallo and de Dios, 2018).

The secondary porosity developed in a storage is the result of mechanical processes: compaction, plastic and brittle deformation, fracturing; and geological ones: dissolution, precipitation, volume reductions by mineralogical changes (Schön, 2015). As in the oil industry, the injection and production of fluids can be improved by increasing secondary porosity with fracking techniques that allow the interconnection of the pores through processes of hydraulic fracturing (Yan et al., 2015) or fracture acidizing (Portier et al., 2007).

The use of $scCO_2$ as a non-aqueous fracturing fluid to increase the production of hydrocarbons in oil and gas fields decreases the necessary water resources. It is presented as a safer option regarding the use of acids by decreasing the required injection pressure, with greater formation stability and less environmental impact. $ScCO_2$ for the production of hydrocarbons presents (Middleton et al., 2015), among other advantages, an increase in the generation and propagation of fracturing with a lower injection rate, being able to generate more extensive and complex fracture networks than water-based working fluids. The use of $scCO_2$ against water enables a greater development of fractures, the permeability of fractured rocks increases with fracturing with $scCO_2$, resulting in three orders of magnitude higher than hydraulic fracturing (Jia et al., 2018; Wang et al., 2017; Middleton et al., 2015; Kim and Moridis, 2015). Furthermore, in the presence of shale, water can alter the mechanical properties of clay-rich shale reservoir formations, reacting with minerals and closing the fractures created during the fracturing operation, reducing the stimulation efficiency (Jia et al., 2018).

Acidizing is one of the most effective and widely means used of oil and gas operators to stimulate well productivity (Yuan et al., 2015; Yue et al., 2018; Zhao et al., 2018; Li et al., 2015; Folomeev et al., 2014; Carpenter N.F., 1962). Stimulation treatments can yield impressive production increases in many wells if properly applied. Although the type of formation will determine the acids that must be used, its permeability influences the pressure required for pumping (American Petroleum Institute, 2014).

The study of the fractured rock massifs permeability has been carried out by means of on-site measurements, laboratory tests, theoretical derivation and numerical simulation. Using high-pressure injection tests to characterize the hydraulic properties of fractured rock strata (Chen et al., 2015b).

With the injection of CO_2 in the geological formations the balance of the system is altered, where once CO_2 is dissolved in the formation fluid two processes can be developed: the solubility trapping (Abba et al., 2019) and the mineral trapping. In the first, with a decrease in
76 pH, CO_2 is trapped in its ionic species (CO_3^{2-} and H^+), taking place the dissolution of the oxides and carbonates on a time scale of days/weeks, which may produce variations in porosity and permeability (Kampman et al., 2014, Lamy-Chappuis et al., 2013). In the second, these reactions increase the alkalinity of the CO_2-brine mixture, generating the subsequent precipitation of carbonates on a weeks/months time scale (Kampman et al., 2014). This phenomenon facilitates the geochemical interaction between the formation fluids, the storage rock and the seal rock (Mitiku et al., 2013, Holzheid, 2016a), giving rise to the mineral trapping (Ketzer et al., 2009, Soong et al., 2004).

During the CO_2 sequestration, the saturated brine dissolves the intergranular cement, producing a detachment and entrainment of fines in the direction of flow, by injection or by the interfacial tension acting on the particles at the CO_2-brine interface (Othman et al., 2018b). The interfacial tension that is a function of wettability is determined both by the mineralogy of the storage (Zhang, X. et al., 2020) and by the state (gas, liquid or supercritical) in which the CO_2 is injected (Peysson et al., 2014; Valle et al., 2018; Yang et al., 2005).

The relationship between the permeability and the pressure drop allows predicting the injection rate in the aquifer and, where appropriate, the productivity of the reservoir. To know the existence of permeability in a formation, it is necessary to establish an injection or production flow with a constant pressure drop. The presence of interconnected pores allows the fluids to flow (Miao et al., 2015, Landau et al., 1987, Nazridoust et al., 2006), otherwise fluctuations or pressure peaks occur due to the absence of effective porosity or the existence of preferential channels that can change due to the drag of fines. In the injection process into the reservoir, the mineral particles present can be detached, being suspended in the injected fluid and, when their size allows, strain in the pore throats during transport. This results in a significant decrease in the permeability of the porous medium due to the process known as fines migration, which can significantly influence the capacity of the injection wells by supplying fluid to the reservoir (Othman et al., 2018a; Othman et al., 2018b).

The negative effect of fines migration on the formation permeability is one of the physical mechanisms that most affect wells (Russell et al., 2017; Khilar and Fogler, 1998; Civan, 2007; Farajzadeh et al., 2016), oil wells (Barkman et al., 1975; Zeinijahromi et al., 2016), gas wells (Byrne and Wagoner, 2009) and surface aquifers of drinking water (Prommer et al., 2013).

Several laboratory studies show a decrease in permeability with high injection/production flow rates (Khilar and Fogler, 1998; Zheng et al., 2014; Russell et al., 2018) because the drag force generated causes the migration of the adhered fines and the decrease in production and injectivity in high ratio wells. Operations carried out in a porous medium containing fine particles susceptible to detachment or entrapment are potentially prone to fines migration.

Directional permeability in natural fractured networks is significantly dependent on the geomechanical properties of fractures (Liu et al., 2016). The preferential flow paths that develop despite their relatively low matrix permeability are governed by the characteristics of the connected fracture networks (Chen et al., 2015 a).

This work investigates the effectiveness of the injection of $scCO_2$ enriched brine in two limestone and dolomite formations that present natural fractures, capable of constituting a CO_2 storage. This action modifies the petrophysical parameters of porosity and permeability and ensures the injection into the aquifer without compromising the tightness of the storage in the long term, compared to the fracture acidizing methods used in the oil industry.

2. Materials and methods

2.1. Materials

The samples studied belong to a deep saline aquifer that can store CO_2. It is enclosed in the sothern section of the Mesozoic Basque-Cantabrian Basin, named "Plataforma Burgalesa". This domain is located in the northern junction of the Cenozoic Duero and Ebro Basins, forming an ES-dipping monocline bounded by the Sierra de Cantabria thrust to the North and the Ubierna Fault System to the South (Tavani, 2012).

The site represents structural dome where the pair seal-reservoir is located within Jurassic Formation (Marly Lias and Sopeña respectively) (de Dios et al., 2018). From a stratigraphic perspective, the Mesozoic succession in the structure starts with the evaporated and clays of the Triassic Keuper Facies, which forms the core of the target dome. The Lower Jurassic is composed of evaporates, dolomites and marls, and lies over Keuper Facies (Quesada et al., 2005). The upper part of the Lower Jurassic and the Middle Jurassic series is constituted by shallow marine carbonates and hemipelagic ramp sediments. The Purbeck Facies (Late Jurassic- Early Cretaceous in age) are formed by clays, sandstones and carbonate rocks placed uncomformably on top of the Jurassic marine rocks. The Lower Cretaceous succession is completed by siliclastic sediments of the Weald Facies, and the Escucha and Utrillas formations. They are made of fluvial deposits that alternate the channel filling sandstones and flood plain shale sediments. The uppermost rocks exposed in the area are Upper Cretaceous carbonates and Cenozoic rocks (lacustrine and detritic) lying uncomformably over the Mesozoic successions (Alcalde et al., 2014).

Overburden is formed of Dogger, Purbeck and Weald and the underlying seal is located at Triassic Keuper (Rubio et al., 2014). Reservoir is Sopeña Formation (120 m thick) comprised of limestone at its upper part and dolomites at the bottom (Kovács, 2014). The storage rock consists mainly of carbonates comprising the geological formations (Fd), Sopeña Calizo (SC) and Sopeña Dolomítico (SD).

The geological complexity of the study area, which has undergone a very complex and tectono-sedimentary evolution has developed fractures under successive deformation stages, either increasing or decreasing its secondary porosity and permeability (Alcalde et al., 2014).

A well that crosses the seal and the storage, allows to extract a core and drilling, parallel to bedding, six samples from it, located at a depth around 1500 m (Rabbani et al., 2018; Doughty, 2006). Table 1 shows their characteristics, dimensions and porosity (measured in AccuPyc II 1340 Pycnometer).

Table 1. Dimensions and porosity of the samples.

Sample		Depth	Weight	Length	Diameter	Volume			Grain Density	Porosity
ID	F_d	(m)	(g)	(mm)	(mm)	Total cm^3)	Solid (cm^3)	Pore(cm^3)	(g/cm^3)	(%)
A1	SC	1448.3	204.42	67.41	37.90	76.03	75.86	0.17	2.69	0.22
A2	SC	1449.7	218.31	71.87	37.84	80.82	80.36	0.45	2.71	0.56
A3	SD	1518.5	217.61	72.24	37.86	81.31	76.61	4.69	2.84	5.77
A4	SC	1442.1	186.38	72.89	37.96	82.50	65.84	16.65	2.83	20.18
A5	SD	1525.7	230.39	74.06	37.82	83.20	81.28	1.91	2.83	2.30
A6	SC	1443.8	213.83	72.11	38.02	81.85	76.88	4.96	2.78	6.06

ID: sample identification; F_d: geological formation Sopeña Calizo/Dolomítico (SC/SD)

The target Jurassic formations are formed by a dolostone unit known as “Carniolas” and an oolitic limestone. The estimated porosity (well log) of the Carniolas reaches over 12% and is slightly lower at the Carbonate Lias level (8.5% in average) (Ogaya et al., 2013).

The selection of the field samples in this research avoids the lack of correspondence between the results of the petrophysical tests carried out in analogues or indirect methods (Ogaya et al., 2013; Márquez and Jurado, 2011) and those coming, as in this case, from materials in depth (Wang et al., 2013).

2.2. Experimental setup

Each rock samples, previously saturated in brine and placed in the triaxial cell in the ATAP experimental facility (Valle and Martínez, 2015) (Fig. 1), was subjected to one of the injections of HCl, HCl-Acetic (CH_3COOH) and Brine-scCO_2 mixture, respectively. During the test, the pressure and temperature conditions, characteristics of the aquifer under study as well as the concentrations of the fluids that will be injected into the samples, were established (American Petroleum Institute, 2014).

The sample (01), saturated in brine, is covered with a thermo-shrinkable plastic (02), which prevents the diffusion of CO_2 towards the radial confinement glycerin. On the outer viton sleeve (03), using the hydraulic group with glycerin (04), the radial confining pressure is established (135/141 bar).With the axial hydraulic group (05), the glycerin pressure is increased, which causes the displacement of the piston (06) generating the axial stress (135/141 bar). In this way, a triaxial confining pressure is established in the rock-fluid system corresponding to the depth of the samples. The oven (07) allows to reach the temperature related to geothermal gradient (44/46 °C), so this temperature and the back-pressure equipment (08), which is used during scCO2/brine injections, ensure respectively a temperature of 31 °C and an injection pressure (P_f) above 74 bar, necessary conditions for injecting CO2 in the supercritical state throughout the test. The test fluids are collected at the outlet in the separator (09) under atmospheric conditions, where the volume of the liquid is measured, and CO2 gas is separated and sent to the gasometer (10) located after the production fluid collector or separator to measure its volume. The gas phase (CO2) exits through the upper part of the separator and reaches the gasometer where the volume produced is measured and recorded. A membrane type sensor (11) measures the incremental pressure (ΔP) between the injection and production surface of the sample. When the pressure sensor limit of 23 bar(ΔP) is reached, the bypass valve (12) opens, allowing the system to be depressurized, preventing injection fluid from passing through the sample, connecting directly to the production line.

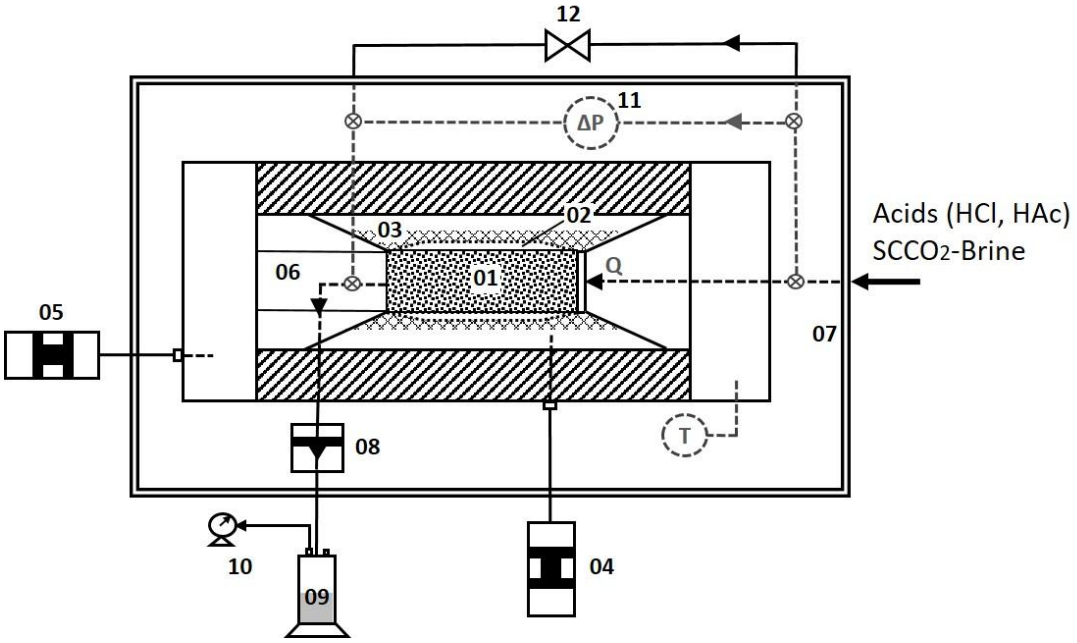

Fig. 1. Experimental ATAP system (Valle and Martínez, 2015): Rock sample (01), Thermo-shrinkable Sleeve (02), Viton sleeve (03), Radial pump to confine glycerine (04), Axial pump to confine glycerine (05), Axial piston (06), Controlled temperature oven (07), Back pressure, BPR (08), Separator (09), Gasometer (10), Pressure difference (11), and Bypass (12).

The data of the tests are recorded and subsequently interpreted using numerical models (Lenormand et al., 1988) in the settings made with the Cydar™ software (Lenormand, 2012).

2.3. Experimental procedures

The study of the material from both formations, carried out in the laboratory, includes a previous characterization stage. A plug is drilled from each of the 6 samples and the end trims are preserved. Of these end trims, a disc corresponding to the injection surface (sample disc) is used for the mineralogical characterization of the sample (Fig. 2 characterization) and the plug is used for petrophysical characterization (Fig. 2 pre-injection measurements) and injection tests (Fig. 2 injection).

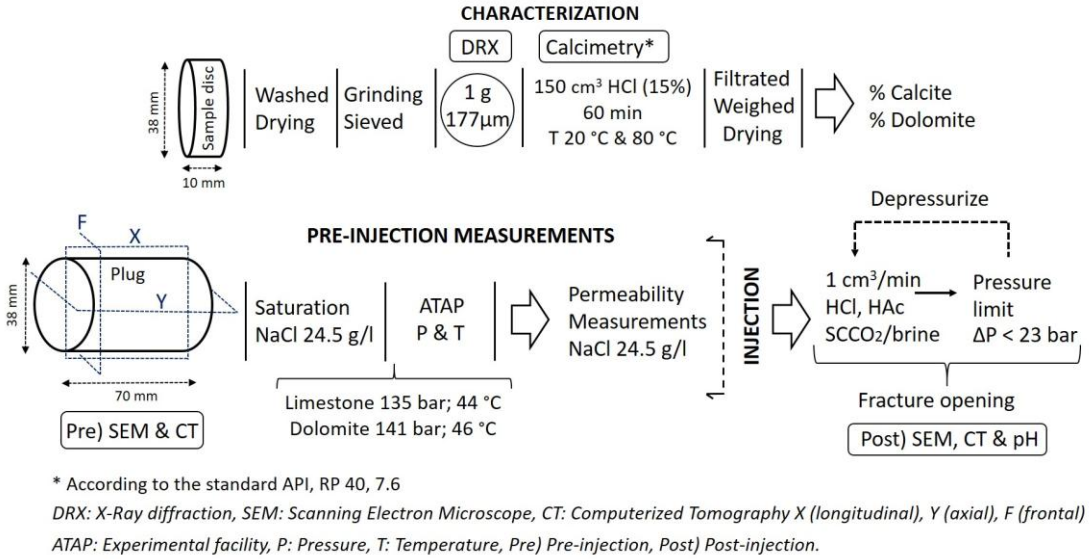

Fig. 2. Diagram of characterization tests, pre-injection measurements and injection into samples.

2.3.1. Sample disc characterization

A disk with dimensions of approximately 10x38 mm corresponding to injection surface of each sample is washed, dried, grinded and sieved, and then analyzed by XRD and calcimetry tests (20/80 °C), to determine its mineralogy and its percentage contents of calcite and dolomite (Fig. 2 characterization).

The major mineral compounds present on the surface, where the injection of each sample is carried out (injection surface), were determined (rough determination) using XRD (Table 2). The geological host formation of the samples, SC or SD, does not determine its principal content in calcite or dolomite, in both cases varying its proportions, and even as in the case of the sample A4 (SC) no calcite content is detected close to the injection surface.

Table 2. Major mineral compounds of the injection surface (sample disc). XRD

Sample		Calcite	Dolomite	Quartz	Anhydrite
ID	F_d	$CaCO_3$ (%)	$CaMg(CO_3)_2$ (%)	SiO_2 (%)	$CaSO_4$ (%)
A1	SC	91.6	7.6	0.7	-
A2	SC	55.5	4.1	3.5	-
A3	SD	-	95.1	0.1	4.8
A4	SC	-	99.1	0.9	-
A5	SD	-	90.5	0.2	9.3
A6	SC	19.9	79.6	0.5	-

ID: sample identification; F_d: geological formation Sopeña Calizo/Dolomítico (SC/SD)

The calcimetry or solubility test to the acid (API standard, RP 40, 7.6) determines gravimetrically the sensitivity of the formation to react with acid. The results are used to determine the volumes of acids required in the field to ensure success in acid stimulation and damage transmitted to the formation (American petroleum Institute, 2014).

Table 3 shows the partial and final results of the calculations corresponding to the calcite and total carbonate content of the samples.

Table 3. Percentage in calcite and total carbonate of the samples (RP40, 7.6).

Sample		W_s (g)		W_s + dry filter (g)		Calcite %	Carbonate %
ID	F_d	20 °C	80 °C	20 °C	80 °C	20 °C	80 °C
A1	SC	1.022	1.016	0.149	0.148	93.83	93.89
A2	SC	1.040	1.087	0.171	0.168	91.82	92.08
A3	SD	1.057	1.100	0.101	0.097	98.48	98.90
A4	SC	1.009	1.004	0.126	0.125	86.85	95.80
A5	SD	1.010	1.069	0.112	0.111	97.33	97.47
A6	SC	1.094	1.090	0.154	0.153	90.42	91.75

According to the standard API, RP 40, 7.6

ID: sample identification; F_d: geological formation Sopeña Calizo/Dolomítico (SC/SD); W_s: sample weight

2.3.2. Plug characterization

A cylindrical plug with dimensions of approximately 70x38 mm, which is washed to remove its content in brine and/or drilling mud, is obtained from each sample in the pre-injection stage (Fig. 2 pre-injection).

The injection surface is studied using Scanning Electron Microscopy with Energy Dispersive X-Ray Spectroscopy (SEM-EDX) in the positions of interest that present visible open/filled fissures to the naked eye or changes in mineralogy. After drying it in an oven and measuring its porosity, different points are selected within the determined position to run SEM for obtaining high and low-magnification images and its spectra with EDX. The precise positions of the plugs are fixed longitudinal X (19 mm), axial Y (19mm) and frontal F (injection surface) sections. The surface and the interior of the sample are analyzed by Medical Computed Tomography (CT)

(Somatom-Siemens Sixteen-row multislice spiral, cutting thickness 0.6 mm with reconstruction increments 0.1 mm; FOV 50 cm, 20-345 mA and 80, 110, 130 Kv) prior to injection (Fig. 2 pre-injection measurements).

Both SEM and CT studies are repeated on the positions fixed in the plugs after the acid and $scCO_2$-brine mixture injections, observing changes and evolution of the fissures (Fig. 2 injection).

2.3.3. Pre-Injection measurements

The plugs, once they are characterized, are saturated in brine (24.5 g/l) and placed in the ATAP device, where conditions corresponding to the depth of the formation, the confining pressure (135/141 bar) and temperature (44/46 °C), are set. Under these conditions, the sample undergoes the brine injection process (Fig. 2 pre-injection measurements). Its permeability, k (mD), to liquid (brine with the same conditions) is measured using Darcy's Law in laboratory units [q (cm^3/s), A (cm^2), μ (cP), L (cm) y ΔP (bar)] (Soulaine, 2015; Agnaou, 2017; Wang and Reed, 2009; Zhao et al., 2011), which is expressed according to Eq. 1.

$$k = - \quad — \tag{1}$$

Darcy's Law for a single phase and steady state radial flow through a porous medium (Fig. 3), in field units [v(ft/s), q (bbl/day), A (ft^2), k (D), μ (cP), dP (psi), dr (ft)], is expressed according to Eq. 2.

$$- \qquad - — \tag{2}$$

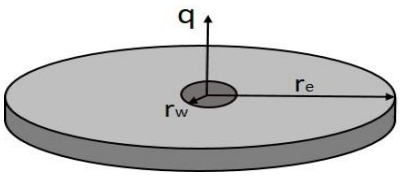

Fig. 3. Diagram of radial flow to the producer/injector well.

If fluid flows through fractures is assumed to be laminar flow, the flow rate along the flow direction through a fracture can be described by the famous “cubic law” or Poiseuille’s equation (Chen et al., 2015a; Miao et al., 2015; Landau and Lifshitz, 1987; Nazridoust et al., 2006) Eq. 3:

$$——— \tag{3}$$

Absolute permeability is a variable in all flow equations, therefore, for its correct estimation, it must be expressed in these equations as a function of effective overburden pressure (P_e) (Chen et al., 2015b).

The average lithostatic (overburden) pressure (P_{ob}) composed of the combined pressure from interstitial fluids (P_f) and the grain-to-grain stress of the rock matrix (P_e), Eq. 4 (Erle and Wagi, 2008) remains constant in all injections thanks to the hydraulic groups (Fig. 1, (04) and (05)). They allow to maintain the radial and axial pressure respectively in the set points values stablish for each of the SC and SD Formations, according to the gradient depth (135/141 bar) (de Dios et al., 2017).

$$P_{ob} = P_f + P_e \tag{4}$$

In this way, the injection pressure increase (P_f) is offset by the decrease in pressure that supports the rock (P_e). An accurate permeability-effective stress ratio can be determined Eq. 5

using a tri-axial compression cell (Fig. 1) (API RP40-6.24) capable of generating pore pressure and axial and radial stress (Eq. 4) (Shi et al., 1986; Dong et al 2010):

(5)

However, since it is not possible to measure the k_0, it is also not possible to calculate the k_e using the pressure ratio P_e/P_0. What is achieved is to apply these pressures to the sample in the ATAP equipment (Fig.1).

2.3.4. Injection

Once the injection of brine into the sample has been carried out, the continuous injection of acid mixtures and $scCO_2$/brine is carried out at a constant flow rate of 1 cm^3/min. This flow rate is selected due to the low absolute permeability and the size of the samples (10 times the diameter of the samples from the study by Al-Khulaifia et al., 2018). The injection process was performed continuously compared to the batch injection by Holzheid, 2016b. The composition of the mixtures injected into each sample is shown in Table 4.

Table 4. Type of injection in each sample.

Sample	Injection mixture
A1 (SC)	10 % HCl
A2 (SC) & A3 (SD)	15 % HCl
A4 (SC)	10 % HCl & 10 % Acetic (CH_3COOH)
A5 (SD) & A6 (SC)	50 % $scCO_2$ & 50 % brine

The incremental pressure between the injection-inlet/production-outlet surfaces is registered. Production is verified through the flow line downstream of the core holder that guides the fluids to the separator, thereby ensuring the circulation of fluids through the sample. When the maximum of the differential pressure sensor (23 bar) is reached, the injection is stopped and the system is depressurized by opening the bypass valve. The process is repeated as many times as necessary until fluid production is achieved.

Injectivity is defined as the ability of a geological formation to accept fluids via their injection through a well (Park et al., 2019). Conceptually, injectivity can be expressed by an index, II, that is represented by the ratio of the injection flow rate to the pressure difference between the reservoir and the wellbore (Fig. 3). It can be described as Eq. 6 for the radial geometry under the steady state condition (Dake, 1983):

(6)

If this Injectivity Index is applied to the samples assuming laminar flow through fractures (Eq. 3) and the maximum ΔP reached between the injection face and their production, results Eq.7:

(7)

This Index allows to compare the aquifer injectivity after acid or $scCO_2$/brine injection.

3. Tests and results

3.1. Pre-injection measurements

During the brine injection into the samples (NaCl 24.5 g/l) at the fixed flow rates (0.2, 0.5 and 1 cm^3/min) very high pressures are reached, which, however, cannot stabilize the differential pressure. The low production of brine with an unstable incremental pressure and above the

limit of the pressure sensor, indicates in all cases that the absolute permeability (k) is less than 0.1 mD (Lenormand, 2012; De Dios et al., 2017).
The results of the tests conducted confirm the low permeability data obtained in the in situ well testing (de Dios et al., 2017). The permeability of the formation was in the range of 0.0063-0.286 mD for a depth of 1439.1-1500.8 m. Besides, the low injectivity during the test development is evident and verifies the one obtained during the Connectivity Test Inter-Wells (CTIW) (de Dios et al., 2017).

3.2. Injection process

The injection of acid mixtures through the samples (Table 4) was carried out within the experimental ATAP system (Fig. 1 and Fig. 2 injection). Figures 4-7 show the records of the pressure sensors (Pinj, ΔP) obtained during the entire injection process at a constant flow rate of 1cm^3/min until, if it happens, reaching the limit of the incremental pressure (23 bar). The injection process is stopped at that moment and the system is depressurized by opening the bypass.

It was not possible to stabilize the pressure drop (ΔP) in any of the samples, probably because the existing micro-fissures act as preferred pathways. As stated in Eq. 3 there is proportionality between the pressure drop in the fissures and the injected flow that circulates through them.

3.2.1. Injection pressure evolution results

10% HCl and 15% HCl injections

In sample A1 (SC), the 10% HCl injection was carried out for three cycles until a maximum injection pressure of 34 bar was reached in the second cycle, with pressure fluctuations due to internal circulation of part of the acid. The injection pressure is maintained in a similar range in the three injection cycles with the exception of the last cycle, where it drops to 9 bar with a small production of acid (Fig. 4).

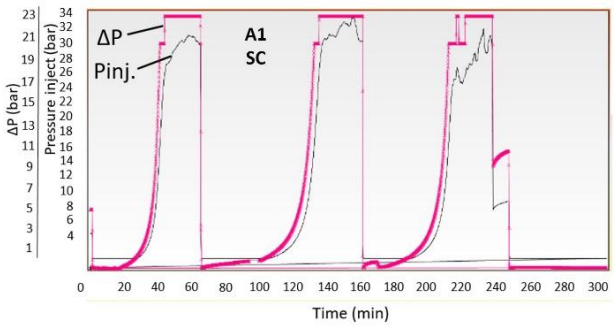

Fig. 4. Injection of 10% HCl (A1).

In samples A2 (SC) and A3 (SD), the injection of 15% HCl is carried out for 4 cycles in both cases. The injection pressure in sample A2 (SC) reaches a peak of 95 bar in the second cycle, probably due to the momentary collapse of the injectivity due to the clogging of the pores (Eq. 3), keeping the rest around 35 bar. On the other hand, in sample A3 (SD) the injection pressure reached in the first two cycles is 32 bar, with a decrease to 20 bar in the third cycle, after an improvement in the sample's injectivity, and an increase up to 42 bar in the fourth one due to the collapse of such injection (Fig. 5).

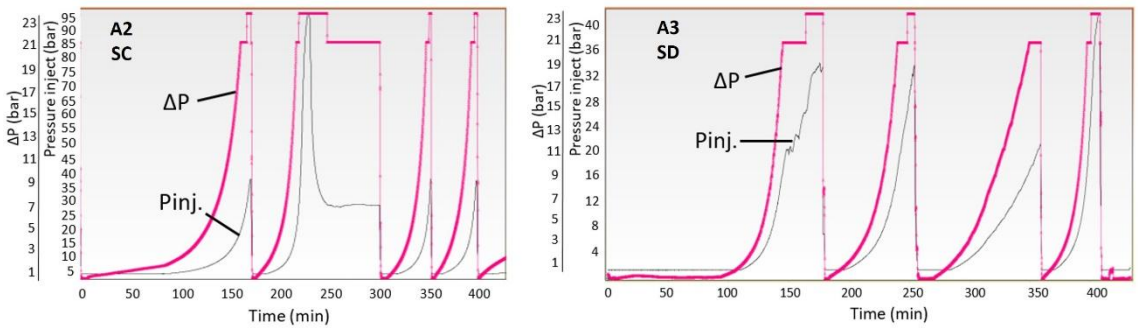

Fig. 5. Injection of 15% HCl (A2, A3).

HCl 10% and Acetic, CH_3COOH 10% injections

The injection of the mixture 10%/10% HCl/Acetic was carried out in sample A4 (SC). The injection has a constant low pressure for more than 60 minutes, and a subsequent rise with fluctuations until reaches the injection collapse at 70 bar and 220 min. Since injection has been possible without reaching the limit of the pressure sensor during this time, once it is reached the system is depressurized and no new injection is performed (Fig. 6).

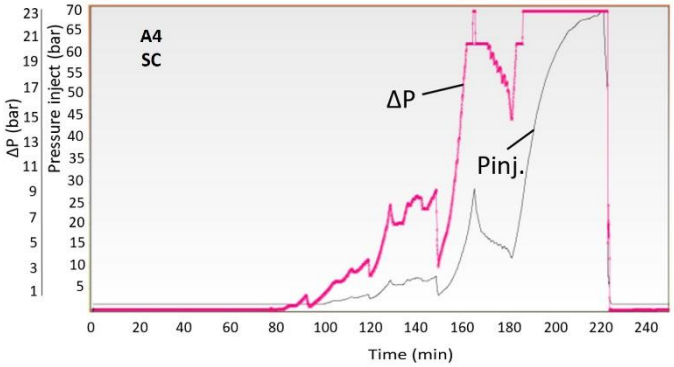

Fig. 6. Injection of HCl 10% and HAc 10% (A4).

$scCO_2$ 50% and brine 50% injections

In samples A5 (SD) and A6 (SC) the injection of the mixture 50%/50% $scCO_2$/brine was carried out with a back pressure adjustment (BPR) and an offset pressure of the system at 74 bar ensuring the maintenance of the supercritical conditions.

With the injection of the $scCO_2$/brine mixture, the pressure sensor limit is not reached in any of the tests carried out on each of the samples. Therefore, it is not necessary to depressurize the system at any time. In addition, the injection pressures reached a maximum of 8.5 bar (relative, offset) in sample A5 (SD) and 15 bar (relative, offset) in sample A6 (SC), with a progressive decrease until the beginning of CO_2 production (10 min after starting the injection). At this time a slight rise in pressure occurs, to decrease slightly as the $scCO_2$/brine mixture passes through the sample.

The continuous decrease in pressure from the start of the injection without the presence of peaks confirms that there is circulation of the mixture through the sample without collapse of the pores (Fig. 7).

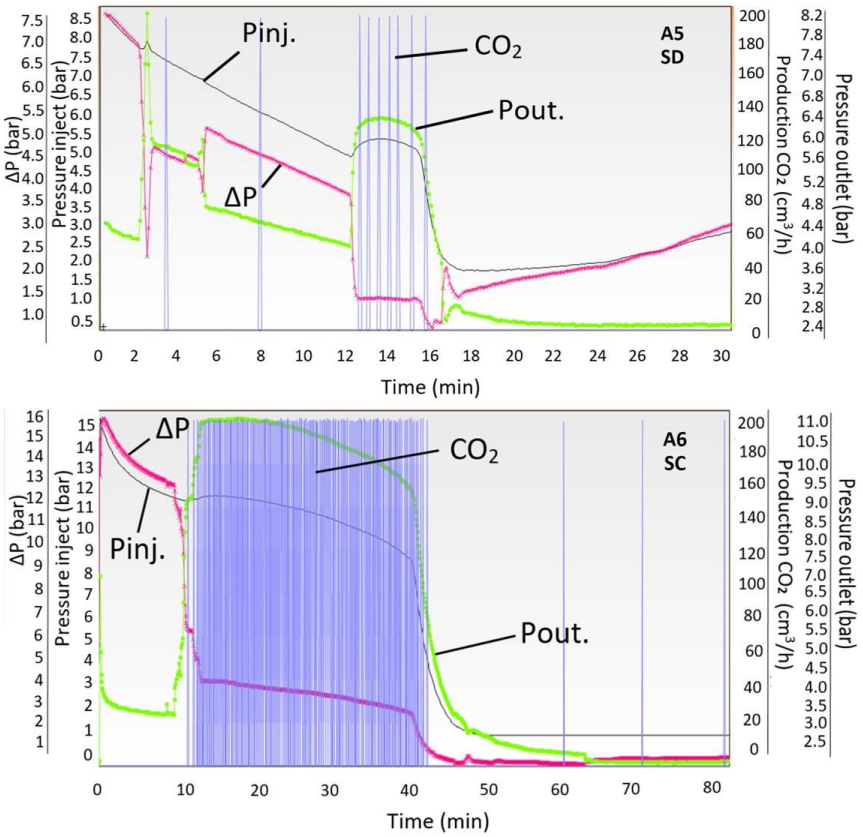

Fig. 7. Injection of brine 50% and $scCO_2$ 50% (A5, A6).

3.2.2. Injectivity Index

The Injectivity Index (Eq. 7) is calculated for each one of the injections made in the samples, obtaining the values collected in Table 5 for the maximum incremental pressure and a constant injection flow rate of 1cc/min.

Table 5. Injectivity Index (II) for each of injections made in the samples.

Plug	Injection fluid	ΔP (bar)	II
A1	10% HCl	34	0.029
A2	15% HCl	95	0.010
A3	15% HCl	42	0.023
A4	10% HCl + 10% CH_3COOH	70	0.014
A5	50% $scCO_2$ + 50% brine	8.5	0.117
A6	50% $scCO_2$ + 50% Brine	15	0.060

Table 5 shows for samples (A1-A4), where acid injection has been carried out, an Injectivity Index (II) average value of 0.02 with a ΔP of 60.2 bar, compared to 0.09 obtained with the injection of $scCO_2$/brine mixture for samples (A5-A6) with a ΔP of 11.7 bar.

3.2.3. SEM and CT results

The SEM and CT images (X: longitudinal, Y: axial and F: frontal; Fig. 2) before and after the acid and $scCO_2$/brine mixtures pass through the samples, allow us to observe the effects and the changes they produce in them.

10% HCl and 15% HCl injections

SEM-EDX images of sample A1 (SC) indicate that mineral dissolution has occurred around the potassium aluminosilicates and quartz filling the fissures. The spectra of positions 1 and 2 (Fig. 8 EDX POST) indicate a decrease in calcium and magnesium, main components of the matrix (Table 2), produced by the dissolution of the carbonates. This superficial dissolution is verified in the frontal section (F) of the images obtained by CT, showing in the longitudinal section (X) an interconnection of the fissures in the interior areas of the sample (Fig. 8 CT red circles).

The released quartz grains, less soluble in acid, together with the aluminosilicates are entrained by the injection flow causing the increase and fluctuations of the injection and incremental pressures.

Fine entrainment seems to decrease in the last injection cycle as there is a decrease in pressure (Pinj, ΔP), produced at 240 min (Fig. 4), linked to the production of mixture in the separator. This is when a natural injection process is established through the sample, presumably through the interconnected fissures.

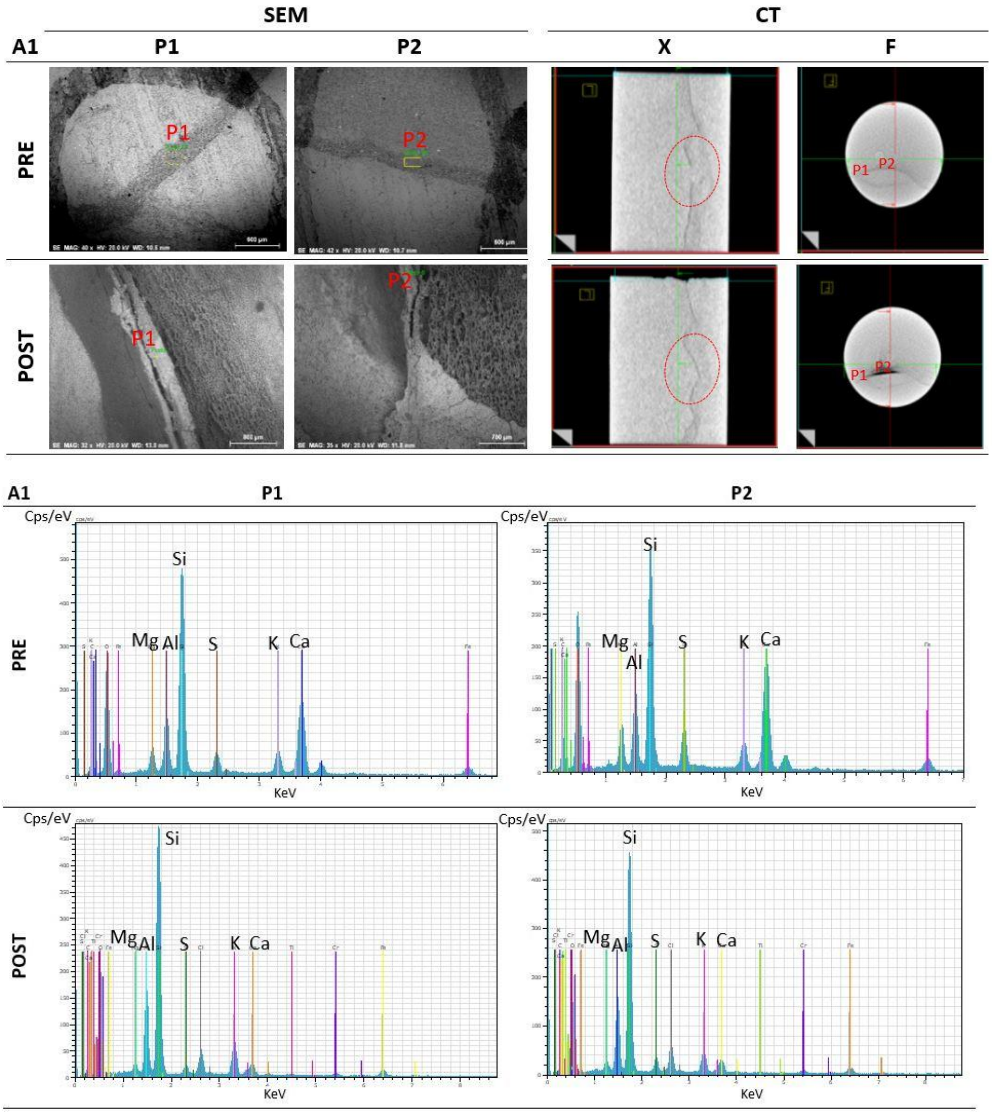

Fig. 8. SEM, EDX (injection surface) and CT sample A1 previous (PRE) and subsequent (POST) to the injection.

The sample A2 (SC) shows fissures filled with potassium and quartz aluminosilicates on its surface (Fig. 9 SEM P1 & P2-PRE), producing after injection a decrease in calcium and magnesium, major components of the matrix. The EDX obtained are similar to those of sample A1 (SC), so they have not been included. The potassium aluminosilicates embedded in the matrix will be free but not dissolved (P1) or partially dissolved (P2) (Fig. 9 SEM POST), as confirmed by CT images (Fig. 9 CT POST red arrows). The increased in injection and incremental pressures confirm the entrainment of potassium aluminosilicate fines by the acidic injection stream (Fig. 5).

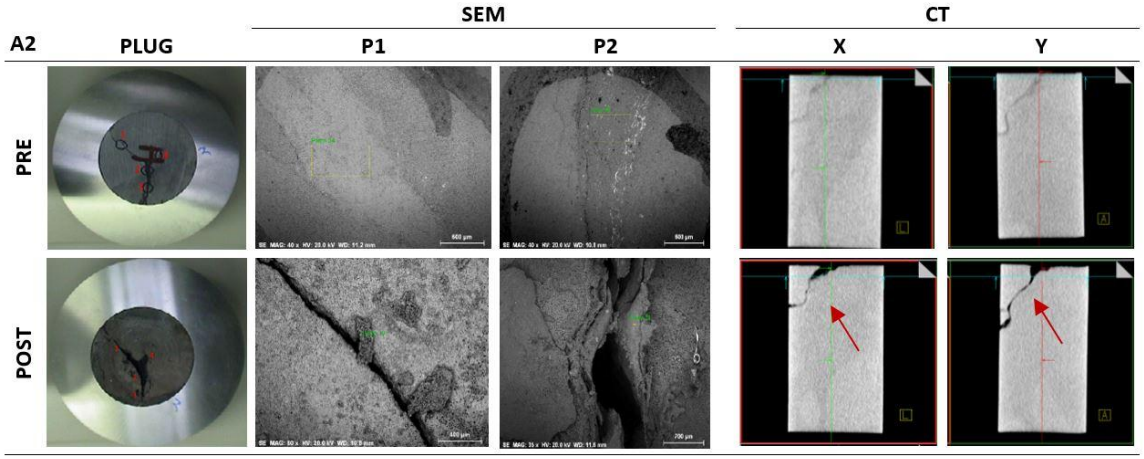

Fig. 9. SEM, EDX (injection surface) and CT sample A2 previous (PRE) and subsequent (POST) to the injection.

In the sample A3 (SD), the absence in a fissure of resistant fillers such as silicates, anhydrite and quartz results in a greater dissolution of carbonates (P1, with high content of calcium and magnesium) (Fig. 10 EDX P1-PRE). Due to the high dissolution produced (Fig. 10 PLUG POST) it was not possible to carry out the SEM study of this area after injection (Fig. 10 SEM P1-POST). A high content of anhydrite has been detected, filling the fissure in position 2 (Fig. 10 EDX P2-PRE), also observed in the XRD of Table 2. Its partial dissolution occurs after the dissolution of the carbonates of the matrix (Fig. 10 EDX P2-POST).

The CT images (Fig. 10 CT Y-POST) show a longitudinal solution that crosses practically the entire sample (enlarged fracture), through which the fine drag characteristic of both fluctuations and increased in injection pressure has occurred (Fig. 5).

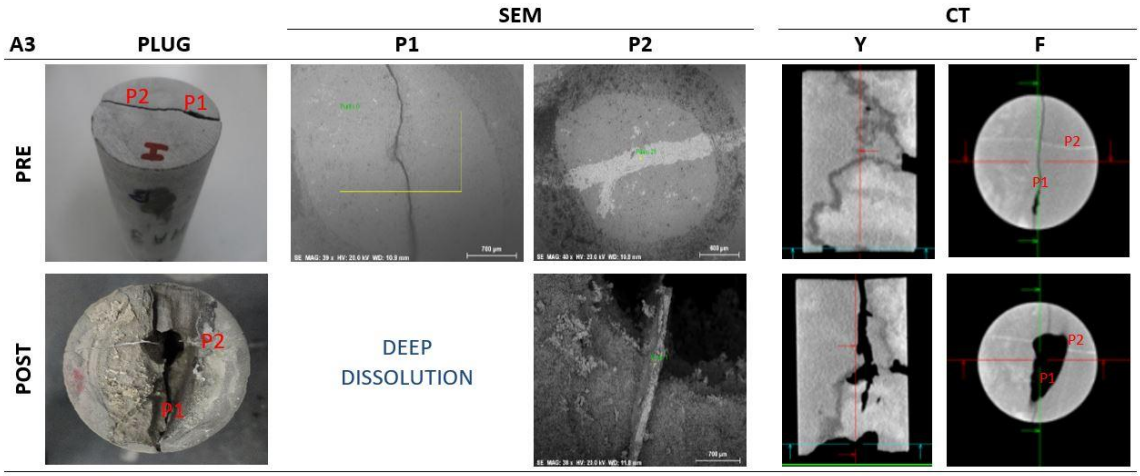

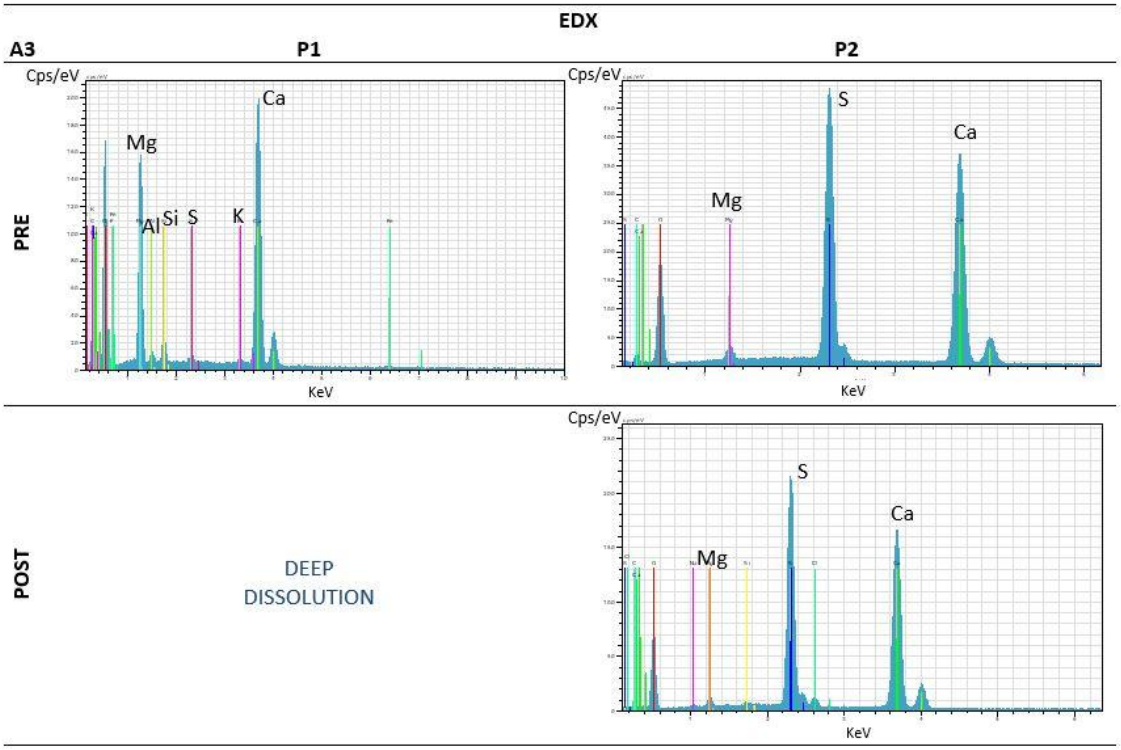

Fig. 10. SEM, EDX (injection surface) and CT sample A3 previous (PRE) and subsequent (POST) to the injection.

HCl 10% and HAc 10% injection

In the sample A4 with primary porosity (Table 1), a single injection with acid production from the beginning was carried out. Although no open fissures are observed in the CT (Fig. 11 CT PRE), the strong surface erosion observed (Fig. 11 PLUG POST) may be the cause of the subsequent collapse produced by the dragging of solids, produced at 220 min (Fig. 6). This dissolution and entrainment coincide both with its low initial pressure and with its fluctuations and increases after the 60 min injection. After the initial dissolution and drag on the injection face (Fig. 11 CT POST red arrow), it is observed that there is no subsequent dissolution due to the collapse of the injection.

The spectrum of position 1 (lighter zone) (Fig. 11 SEM & EDX P1-PRE) indicates the presence of chlorides (Cl) prior to injection (Fig. 11 EDX P1-PRE), causing its dissolution almost complete. On the other hand, the scarce silica that has been initially detected, because it is scattered, has been entrained in the solution produced by the acids (Fig. 11 EDX P1 & P2-PRE).

The erosion of the entire surface (Fig. 11 PLUG & CT POST red arrow) was originated during the injection in A4, thus, spectra at positions 1 and 2 after injection have not been studied.

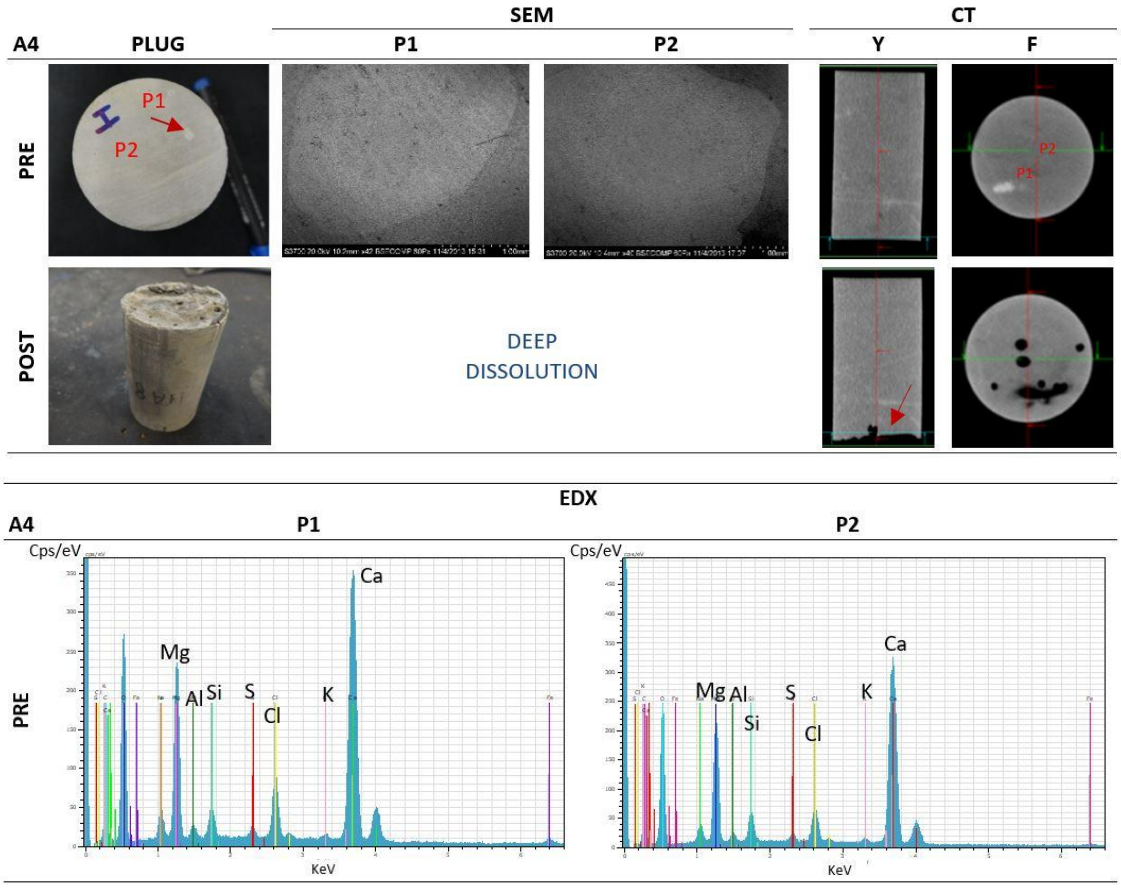

Fig. 11. SEM, EDX and CT sample A4 previous (PRE) and subsequent (POST) to the injection.

scCO$_2$ 50% and brine 50% injections

The SEM and CT images of the samples A5 (SD) and A6 (SC) do not present, except in position 2 (surface) of sample A5, fissure opening (Fig. 12 SEM P2-PRE). However, this solution has not produced solids entrainment since the injection pressure has decreased from the initial 8.5 bar, without fluctuations that indicate collapse, until the moment (at 12 min of injection) in which CO_2 and brine begin to be produced through the production surface (outlet) of the sample (Fig. 7). On the other hand, in the records of the injection pressure of $scCO_2$ enriched brine, the ΔP sensor limit is not reached, thus depressurizing of the system and stopping the injection was not necessary. The production of the mixture at the exit of the sample (production surface) begins within a few minutes of the injection without creating preferential pathways inside the sample and without producing the drag of solids that clog the production line increasing the pressure of the system.

The matrix of sample A5 is made up of carbonates, mostly dolomite, Table 2 (Fig. 12 EDX, PRE). The EDX at position 2 indicates magnesium and calcium concentrations (Fig. 12 EDX P2-PRE) similar to those in sample A4 (Fig. 11 EDX P1-PRE), however, less dissolution was observed with the $scCO_2$/brine injection (Fig. 12 EDX P2-POST) than with HCl and Acetic (Fig. 11 PLUG POST). While the dolomite attack occurs (Fig. 12 EDX POST) the rest of the unaltered grains that are released are dragged away leaving open fissures and superficial holes (Fig. 12 SEM P1 & P2-POST). As a consequence of the presence in the sample of these hollow spaces (Fig. 12 SEM P1-POST red circles) the spectrum of position 1 post-injection could not be performed (Fig. 12 EDX P1-POST). The presence of residual iron sulfide grains identified as bright white dots, seems to indicate that the anhydrite (light gray area) that surrounds them had been

generated as a consequence of its alteration (Fig. 12 SEM P1-PRE).

In position 2, the presence of silica in the fissure facilitates the dissolution of the surrounding carbonates (Fig. 12 EDX P2-POST). Its effect is less than in the case of injection of HCl and Acetic acids (Fig. 11 PLUG POST), also causing entrainment of non-soluble particles (silicates and anhydrite).

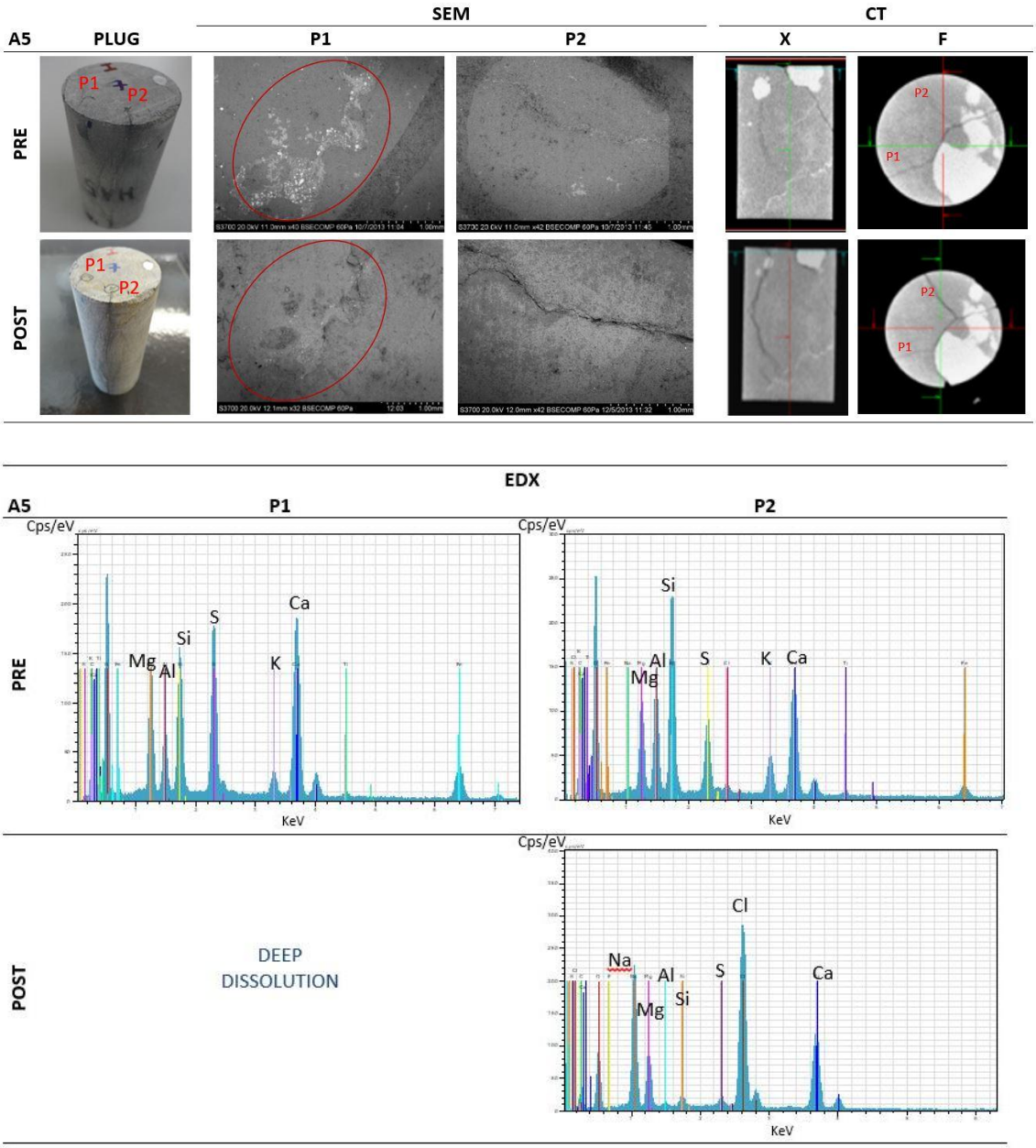

Fig. 12. SEM, EDX (injection surface) and CT sample A5 previous (PRE) and subsequent (POST) to the injection.

The attack that occurs in sample A6 is lighter than in the other injections. The spectrum at position 1 (Fig. 13 EDX P1-PRE) shows the presence of dolomite (DRX Table 2), with some iron sulfides and silicates dispersed in a homogeneous way. The dolomitic matrix appears to be dissolving superficially, with lighter shade silicate and sulfide grains highlighted (Fig. 13 SEM P1-POST). The relative increase of iron, sulfur and silicon occurs, as well as the appearance of chlorine and sodium of the brine (Fig. 13 EDX POST).

The existing sealed fissure in the axial and longitudinal CT image (Fig. 13 CT PRE) is not aligned with the direction of the injection flow, indicating that the fluid has moved through the matrix dissolving the minerals that they surround it (Fig. 13 CT POST, red arrows). The continuous decrease in injection pressure from the initial 15 bar to the production of brine and CO_2 collected in the separator (09) and gasometer (10) respectively, indicates once again that after dissolution, there has been no entrainment of solids that collapse the flow advance (inlet-outlet) towards the production line (Fig. 7).

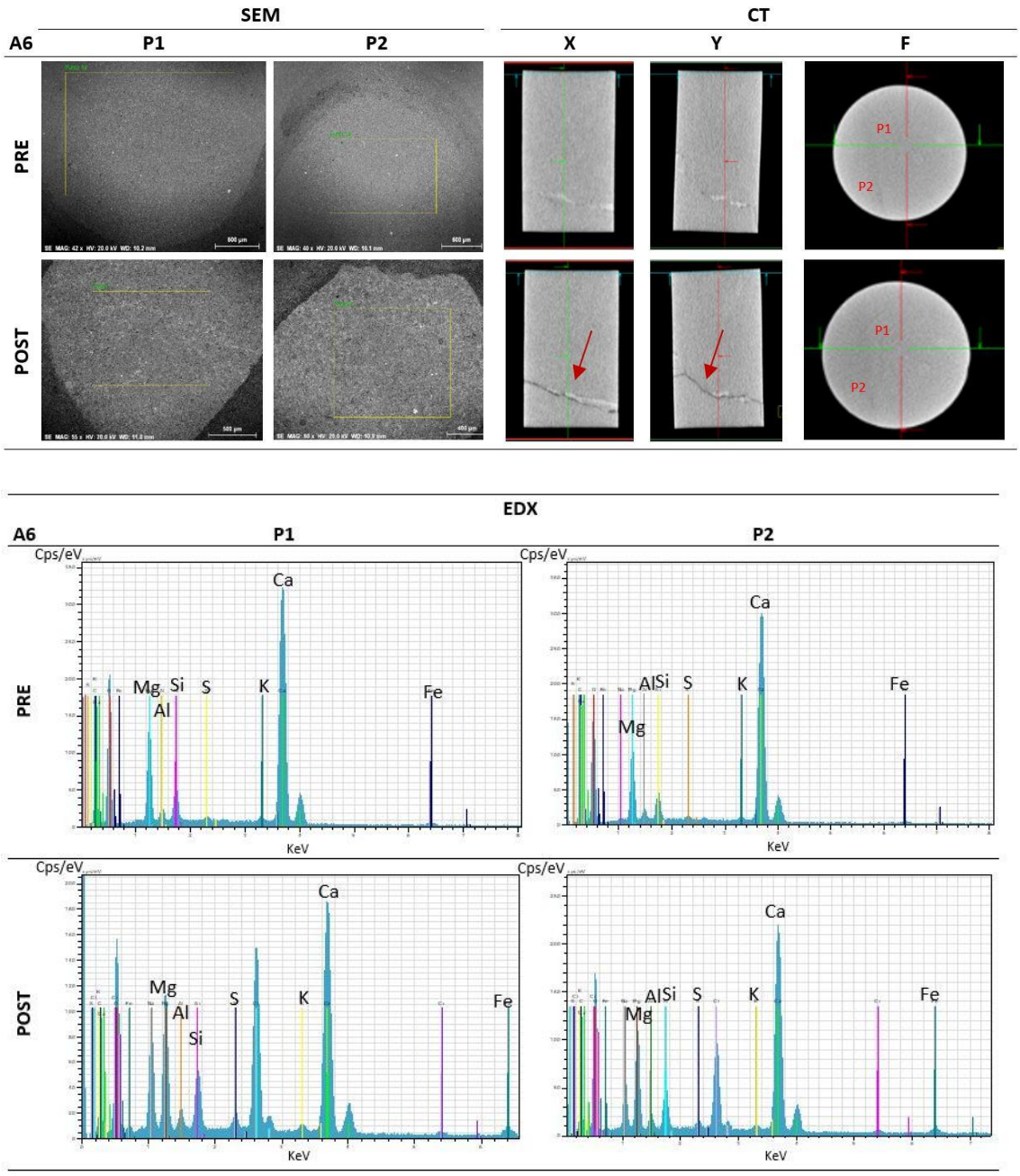

Fig. 13. SEM, EDX and CT sample A6 previous (PRE) and subsequent (POST) to the injection.

The chemical processes are fully dependent on the amount of CO_2 dissolved in brine (André et al., 2007) and the composition of it (Crockford et al., 2014). The aqueous form of CO_2, not the molecular one, is reactive with the storage rock. The solubility of CO_2 is fully dependent on pressure and on temperature and the ionic strength. Solubility of CO_2 is lower at elevated temperature and salinity, and greater at elevated pressure (Rosenbauer et al., 2005;

Rosenbauer and Koksalan, 2002; Duan and Sun, 1996; Takenouchi and Kennedy, 1964) by increasing the hydrophobicity of the reservoir rock (Yang et al., 2008). When the pressure and temperature conditions are constant, a decrease in the solubility of CO_2 in the brine occurs as its salinity increases (Bachu and Bennion, 2009).

In the absence of any reaction with the rock of the aquifer, the dissolved CO_2 results in an acid solution of pH=3.4 due to dissociation of carbonic acid (Rosenbauer et al., 2005). The dissociation of carbonic acid to hydrogen ion (reactive) and bicarbonate $2HCO^{3-} + Ca^{2+}$ initiates a series of complex reactions with the fluids present in the aquifer and rocks to fix CO_2 in the aqueous and mineral phases. The fast dissolution of carbonates is the response to the decrease in pH (Ketzer et al., 2009).

After the injection carried out in the samples A5 and A6, a pH of 4 and 2 was measured in the production of fluids respectively.

When CO_2 is injected into saline aquifer, basically, two types of reactions can occur, those that change the acidity of the formation and those that do not. The ratios of these reactions can vary from formation to formation and at different levels depending on the mineralogy and compositions of the fluids in the aquifer (De Silva et al., 2015). Generally, during the CO_2 injection in saline aquifers, its pH can vary from 3 to 7 close or far away from the injection well, respectively.

4. Discussion

In hydraulic fracturing for the exploitation of hydrocarbon resources, large quantities of fluid are injected under pressure to create and propagate the fractures (Carpenter, N. F., 1962). With fractured acidizing, channels are created in the walls of existing fractures in the rock, which must be partially soluble in the acid used, limiting its application to generally carbonate reservoirs. Acidification according to the usual technique is usually better in shallow, low-temperature reservoirs (less than 90 °C) and with a maximum effective stress on fractures of less than 340 bar (Williams and Nierode, 1972). This reduces the reaction rate of the acid with the formation, allowing it to penetrate the fracture with greater depth before its effect is exhausted.

The reaction of the acid in a carbonate formation causes the release of fines, which occurs when the release torque generated by the hydrodynamic drag force exceeds the coupling torque generated by the electrostatic attraction force (Russell et al., 2018). When the flow velocities are higher, a greater drag force is produced and, therefore, an increase in the extent of the detachment of the particles (Zheng et al., 2014). On the other hand, the electrostatic force decreases when the fluid salinity is lower (Khilar et al., 1983; Shen et al., 2018), or with an increase in pH (Patil et al., 2011), resulting in a higher detachment of particles.

Aquifers with reduced primary or matrix porosity have drawbacks for CO_2 storage, being necessary to act on them to improve their injectivity. Several studies indicate that the effects of injection of CO_2-saturated brine increases matrix porosity in the short term with an intensity that differs depending on whether the CO_2 is in a gaseous or supercritical state (Peysson et al., 2014). Injection of CO_2-saturated brine results in a low pH that can cause dissolution of mineral cement and generation of particles with migration of fines (Othman et al., 2018b)

Mathematically it has been shown (Huang et al., 2018) that wettability influences the interfacial forces acting on fine particles, with their subsequent associated displacement. Capillary forces or wettability can reduce injection when fine migration occurs (Guo et al., 2018; Chequer et al., 2018; Russell et al., 2018), with pore blockage during CO_2 sequestration tests (Othman et al., 2018a).

During the acidification process with acid mixtures in a naturally fractured carbonate aquifer, the migration of fines causes an increase in the pressure drawdown and a decrease in the injection ratio.

From the first stages of injection into the well, a movement of particles occurs that affects predictions based on laboratory tests, where the injection rate obtained can be less than half of the initial value (Russell et al., 2018).

The use of HCl and Acetic acids favors the increase of the secondary porosity of the storage (Van Golf-Racht, 1982), where a higher concentration of HCl causes an increase in the dissolution of the carbonates that causes a greater drag of fines and the consequent blockage of the injection, reflected in the increase in both injection pressure and incremental pressure. The injection of 10% HCl produces the dissolution of the carbonate matrix (Fig. 8), compared to 15% where a dissolution of the carbonates near the fissures occurs (Fig. 9 & 10). In the case of open fissures, the surface free attack produces the appearance of cavities in these areas (Fig. 10), with less dissolution produced when they are filled (Fig. 9). On the other hand, the injection of the HCl/Acetic mixture with a concentration of 10%/10% generates a greater range and less production of cavities as a consequence of the greater dissolution of the matrix (Fig. 11). However, the greater phenomena of dissolution and entrainment of solids cause continuous production blockages, with high injection pressures, which do not allow stabilization (Fig. 6).

The $scCO_2$ injection appears to be weakly reactive, with limited modification of well injectivity. The CO_2 reacts firstly dissolving in the aqueous solution with an increase in the acidity of the brine and the potential mineral dissolution, favoring the increase of the porosity. The injection of brine saturated with CO_2 (Picot-Colbeaux et al., 2009, Farquhar et al., 2015, Pokrovsky et al., 2005) causes the dissolution of calcite, dolomite and anhydrite, with an increase of both the porosity and the permeability and a decrease in the pH of the effluents. The dissolution ratio of the calcite in the rocks depends on the amount of CO_2/brine mixture, the local permeability, which allows the passage and distribution of the acidic brine, and the accessibility to the mineral (Lammy-Chappuis et al., 2013).

The previous results of tests, carried out in surface analogous, in which we have participated, indicated the effect on the porosity of the storage in fractured carbonates when $scCO_2$ was injected with or without impurities. In samples with previous porosity (18.87%), the injection of $scCO_2$ produces an increase in such porosity (21.02%). On the other hand, when the injection contains impurities the mixture is not in a supercritical state, at P and T conditions of pure $scCO_2$, which produces a decrease of the primary porosity from 8.94% to 1.95% (de Dios et al., 2016).

Injecting the pure $scCO_2$ mixture with brine requires lower injection pressures and there are no blockages in the incremental pressure (Fig. 7). The production of brine in the separator and CO_2 in the gasometer ensure a dissolution of the matrix and the consequent increase in secondary porosity without a massive dissolution of the carbonates and fines entrainment (Fig. 13 & 14). The tests of this work carried out the injection of pure $scCO_2$ and brine verifying the production of fluids, and assuming a migration dominated by the existence of fractures (de Dios et al., 2017). In these areas the injection process involved the dissolution of the carbonates that surrounded the aluminosilicates, anhydrite, quartz and iron sulfides that sealed the fractures, with a slight drag of fines.

5. Conclusions

The methodology for the injection of acid mixtures in the ATAP experimental facility, together with the macroscopic observation by means of imaging techniques of the injection surface and the interior of the samples, makes it possible to study a formation for CO_2 storage.

Naturally fractured carbonate formations with low porosity and permeability, due to the fissure filling, are hardly susceptible to constituting a CO_2 store due to their low injectivity and capacity associated. Injection of acidic mixtures with different proportions of HCl, CH_3COOH and $scCO_2$/brine has effects on injection pressures, pressure drop and the production of the corresponding fluids.

The treatments with HCl and CH_3COOH acids have led to an increase in secondary porosity from both dissolution and stress generated as a result of high injection pressures. On the other hand, the dissolution of both the matrix and the components that filled the fissures is achieved with the $scCO_2$/brine injection despite the lower pressure reached, descendant from the beginning. From the start of the injection, CO_2 and brine were produced in the gasometer and separator respectively with negligible pore blockage which represents a smooth increase in the porosity without the occurrence of enlarged fissures.

The capacity of the storage conditioned by the aquifer's injectivity is evaluated by the Inyectivity Index (II). The value obtained confirms the lower pressure increases and increased injectivity obtained with the $scCO_2$/brine injection compared to the injection of HCl and CH_3COOH acids

The injection of HCl and CH_3COOH acids causes a blockage of the pores and the dissolution of the seal and storage rock. This implies a reduction in the permeability of the samples and the opening of enlarged fractures will cause a lack of sealing. In addition, exceeding the fracture pressure makes unsafe storage in the long term. By contrast with the injection of $scCO_2$/brine, the dissolution of the matrix occurs without the opening of enlarged fissures/fractures that could compromise the safety of the storage.

The use of acids involves the use of foreign fluids to the system (brine from the aquifer + CO_2 injected) and the potential risk of affecting the environment, even with sufficient capacity and experience to carry out a safe injection, against the use of $scCO_2$/brine that involves the usage of system fluids without risk of contamination.5

The increase in secondary porosity caused by the injection of $scCO_2$/brine improves the injectivity and rock storage capacity, presenting itself as an economically and technically profitable alternative for the susceptible aquifers to store CO_2. The use of $scCO_2$ enriched brine against the injection of acids to improve the injectivity, supposes a safe operation of storage of CO_2 by the phenomenon of controlled dissolution-precipitation of carbonates, which favors the trap mechanisms of solubility trapping and mineral trapping, ensuring the tightness of the storage.

For a better knowledge of the entrainment phenomenon, the analysis of the concentration of fines in the acidic mixtures or in the brine produced is proposed, as well as a control of the pH variations associated with the chemical reactions developed in the samples.

Acknowledgements

We thank the CIUDEN (Fundación Ciudad de la Energía) for providing us with the samples used in this work from the Hontomín PDT (European Energy Programme for Recovery).

References

Abba M.A., Abbas A.J., Nasr G.G., Al-Otaibi A., Burby M., Saidu B., Suleiman S.M. 2019. Solubility trapping as a potential secondary mechanism for CO2 sequestration during

enhanced gas recovery by CO2 injection in conventional natural gas reservoirs: An experimental approach. Journal of Natural Gas Science and Engineering, 71, 103002. https://doi.org/10.1016/j.jngse.2019.103002

Agnaou, M., Lasseux, D., Ahmadi, A. 2017 Origin of the inertial deviation from Darcy's law: An investigation from a microscopic flow analysis on two-dimensional model structures. Physical Review E. https://doi.org/10.1103/PhysRevE.96.043105

Al-Khulaifia, Y., Lina, Q., Blunta, M. J., Bijeljica, B. 2018. Reservoir-condition pore-scale imaging of dolomite reaction with supercritical CO2 acidified brine: Effect of pore-structure on reaction rate using velocity distribution analysis. Int. J. Greenh. Gas Control 68, 99-111. https://doi.org/10.1016/j.ijggc.2017.11.011

Alcalde, J., Marzán, I., Saura, E., Martí, D., Ayraza, P., Juhlin, Ch., Pérez-Estaún, A., Carbonell, R. 2014. 3D geological characterization of the Hontomín CO2 storage site, Spain: Multidisciplinary approach from seismic, well-log and regional data. Tectonophysics 627, 6-25.

American Petroleum Institute (API). Acidizing treatment in oil and Gas Operators, 2014. Briefing Paper. Digital Media | DM2014-113 | 05.14 | PDF.

American Petroleum Institute (API). Recommended Practices for Core Analysis. Recommended Practice 40. Second Edition, February 1998.

André, L., Audigane, P., Azaroual, M., Menjoz, A., 2007. Numerical modeling of fluid-rock chemical interactions at the supercritical CO2-liquid interface during CO2 injection into a carbonate reservoir, the Dogger aquifer (París Basin, France). Energy Convers. Manage. 48 (6), 1782-1797. https://doi.org/10.1016/j.enconman.2007.01.006

Bachu, S. and Bennion, D.B., 2009. Interfacial Tension between CO2, Freshwater, and Brine in the Range of Pressure from (2 to 27) MPa, Temperature from (20 to 125) °C, and Water Salinity from (0 to 334,000) mg.L−1. Journal of Chemical Engineering Data, 54(3), 765-775

Barkman, J., Abrams, A., Darley, H., Hill, H., 1975. An oil-coating process to stabilize clays in fresh waterflooding operations (includes associated paper 6405). J. Petrol. Technol. 27 (09), 1053-1059. https://doi.org/10.2118/4786-PA

Byrne, M.T., Waggoner, S.M., 2009. Fines migration in a high temperature gas reservoir - laboratory simulation and implications for completion design. In: SPE-121897. SPE European Formation Damage Conference Held in Scheveningen, the Netherland, 27-29 May. https://doi.org/10.2118/121897-MS

Carpenter, N. F. 1962. United States Patent Office. 3252904: Acidizing and Hydraulic fracturing of wells. The Dow Chemical Company, Midland. July 9. Ser. No. 208252.

Civan, F., 2007. Reservoir Formation Damage: Fundamentals, Modeling, Assessment, and Mitigation. Gulf Professional Publishing, Elsevier, Burlington, USA.

Crockford, P., Telmer, K., Best, M., 2014. Dissolution kinetics of Devonian carbonates at circum-neutral pH, 50 bar *p*CO2, 105°C and 0.4 M: The importance of complex brine chemistry on reaction rates. Applied Geochemistry 41, 128-134. https://doi.org/10.1016/j.apgeochem.2013.12.008

Chen, D., Pan, Z., Ye, Z., 2015a. Dependence of gas shale fracture permeability on effective stress and reservoir pressure: model match and insights. Fuel 139, 383-392.

Chen, Y.F., Hu, S.H., Hu, R., Zhou, C.B., 2015b. Estimating hydraulic conductivity of fractured rocks from high-pressure packer tests with an Izbash's law based empirical model. Water Resour. Res. 51 (4), 2096e2118. https://doi.org/10.1002/2014WR016458

Chequer, L., Vaz, A., Bedrikovetsky, P., 2018. Injectivity decline during low-salinity waterflooding due to fines migration. J. Pet. Sci. Eng. 165, 1054-1072. https://doi.org/10.1016/j.petrol.2018.01.012

Dake, L.P., 1983. Fundamentals of Reservoir Engineering. Elsevier Science, Amsterdam.

de Dios, J.C., Delgado, M.A., Marín, J.A., Martinez, C., Ramos, A., Salvador, I., Valle, L., 2016. Short-term effects of impurities in the CO2 stream injected into fractured carbonates. Int. J. Greenh. Gas Control 54 (2), 727-736. https://doi.org/10.1016/j.ijggc.2016.08.032

de Dios, J.C., Delgado, M.A., Martínez, C., Ramos, A., Álvarez, I., Marín, J.A., Salvador, I., 2017. Hydraulic characterization of fractured carbonates for CO2geological storage: Experiences and lessons learned in Hontomín Technology Development Plant. Int. J. Greenh. Gas Control 58, 185-200. https://doi.org/10.1016/j.ijggc.2017.01.008

de Dios, J.C., Le gallo, Y., Marín, J.A., 2018. Innovative CO2 injections in carbonates and advanced modelling for numerical investigation. Preprints 2018. https://doi.org/10.20944/preprints201807.0537.v1

de Silva, G.P.D., Ranjith, P.G., Perea, M.S.A., 2015. Geochemical aspects of CO2 sequestration in deep saline aquifer: A review. Fuel 155, 128-143. https://doi.org/10.1016/j.fuel.2015.03.045

Dong, J., Hsu, J., Wu, W., Shimamoto, T., Hung, J., Yeh, E., Wu, Y., Sone, H. 2010. Stress-dependence of the permeability and porosity of sandstone and shale from TCDP Hole-A. International Journal of Rock Mechanics & Mining Sciences 47, 1141–1157.

Doughty, Ch. 2006. Site characterization for CO2 geological storage and vice versa. The Frio Brine Pilot as a case study. Proceedings; SCCO2 Symposium, California, March 20-22.

Duan, Z., Sun, R. 1996. Geochim. Cosmochim. Acta 6 (20), 3859 -3867.

Erle, C. D., Waqi, A. 2008. Chapter 3- Wettability and production. Wettability, pg 121-172. https://doi.org/10.1016/B978-1-933762-29-6.50009-0

Farajzadeh, R., Lotfollahi, M., Lake, L.W., 2016. Simultaneous sorption and mechanical entrapment during polymer flow through porous media. Water Resour. Res. 52 (3), 2279-2298. https://doi.org/10.1002/2015WR017885

Farquhar, S.M., Pearce, J.K., Dawson, G.KW., Golab, A. Sommacal, S., D. Kirste, D., Biddle, D., Golding, S. M., 2015. A fresh approach to investigating CO2 storage: Experimental CO2-water-rock interactions in a low-salinity reservoir system. Chemical Geology 399, 98-122. https://doi.org/10.1016/j.chemgeo.2014.10.006

Folomeev, A. E., Sharifullin, A.R., Vakhrushev, S.A., Murinov, K.Yu., Akimkin, A.V.,. Lenchenkova, L.E., Nabiullin, R.M., Federov, A.I. 2014. Theory and Practice of Acidizing High Temperature Carbonate Reservoirs of R. Trebs Oil Field, Timan-Pechora Basin. SPE-171242-MS. SPE Russian Oil and Gas Exploration & Production Technical Conference and Exhibition, 14-16 October, Moscow, Russia. https://doi.org/10.2118/171242-MS.

Guo, Z., Vu, P.N.H., Hussain, F., 2018. A laboratory study of the effect of creep and fines migration on coal permeability during single-phase flow. Int. J. Coal Geol. 200, 61-76. https://doi.org/10.1016/j.coal.2018.10.009

Holzheid, A., 2016a. Dissolution kinetics of selected natural minerals relevant to potential CO2-

injection sites- Part 1: A review. Geochemistry 76, 621-641. https://doi.org/10.1016/j.chemer.2016.09.007

Holzheid, A., 2016b. Dissolution kinetics of selected natural minerals relevant to potential CO2-injection sites- Part 2: Dissolution and alteration of carbonates and feldespars in CO2-bearing brines. Geochemistry 76, 643-657. https://doi.org/10.1016/j.chemer.2016.09.008

Huang, F., Kang, Y., You, L., Li, X., You, Z., 2018. Massive fines detachment induced by moving gas-water interfaces during early stage two-phase flow in coalbed methane reservoirs. Fuel 222, 193-206. https://doi.org/10.1016/j.fuel.2018.02.142

Hurtado Bezos, A., 2012. Estimación de la capacidad de almacenamiento geológico de CO2. Metodología e incertidumbres. Editorial Académica Española, 452 pages. ISBN-13: 978-3847355922.

Iding, M., Ringrose, P., 2010. Evaluating the impact of fractures on the performance of the In Salah CO2 storage site. Int. J. Greenh. Gas Control 4, 242-248. https://doi.org/10.1016/j.ijggc.2009.10.016

Jia, Y., Yiyu, L., 2018. Surface characteristics and permeability enhancement of shale fractures due to water and supercritical carbon dioxide fracturing. Journal of petroleum science and Engineering. https://doi.org/10.1016/j.petrol.2018.02.018

Kampman, N., Bickle, M., Wigley, M. Dubacq, B., 2014. Fluid flow and CO2-fluid-mineral interactions during CO2-storage in sedimentary basins. Chemical Geology 369, 22-50. https://doi.org/10.1016/j.chemgeo.2013.11.012

Ketzer J, Iglesias R, Einloft S, Dullius J, Ligabue R, De Lima V. 2009. Water-rock-CO2 interactions in saline aquifers aimed for carbon dioxide storage: experimental and numerical modeling studies of the Rio Bonito Formation (Permian), southern Brazil. Appl Geochem. 24:760-7. https://doi.org/10.1016/j.apgeochem.2009.01.001

Khilar, K.C., Fogler, H.S., Ahluwalia, J., 1983. Sandstone water sensitivity: existence of a critical rate of salinity decrease for particle capture. Chem. Eng. Sci. 38 (5), 789-800. https://doi.org/10.1016/0009-2509(83)80188-2

Khilar, K.C., Fogler, H.S., 1998. Migration of Fines in Porous Media. Kluwer Academic Publishers, Dordrecht.

Kim, J., Moridis, G. J. 2015. Numerical analysis of fracture propagation during hydraulic fracturing operations in shale gas systems. International Journal of Rocks Mechanics & Mining Sciences 76, 127-137.

Kovács, T., 2014. Characterization of the Hontomin reservoir and seal formations. Proceedings of the 4th Spanish-French Symposium on CO2 Geological storage.

Lamy-Chappuis, B., Angus, D., Fisher, Q., Grattoni C., Yardley, B.W.D., 2013. Rapid porosity and permeability changes of calcareous sandstone due to CO2-enriches brine injection. Agu Publications. Geophysical Research Letters. 10.1002/2013GL058534. Res. Lett, 41,399-406. https://doi.org/10.1002/2013GL058534

Landau, L., Lifshitz, E. 1987. Fluid Mechanics. Vol 6. Course of theoretical Physics.

Le Gallo, Y., De Dios, J.C., 2018. Geological Model of a storage Complex for a CO2 storage Operation in a Naturally-Fractured Carbonate Formation. Geosciences 8, 354. https://doi.org/10.3390/geosciences8090354

Lenormand R., Touboul E., Zarcone C. 1988. Numerical models and experiments on immiscible

displacements in porous media. Journal of Fluid Mechanics, 189, 165-187. https://doi.org/10.1017/S0022112088000953

Lenormand R. CydarR. Cydarex, 2012.

Li, N., Dai, J., Liu, Ch., Liu, P., Zhang, Y., Luo, Z. 2015. Feasibility study on application of volume acid fracturing technology to tight gas carbonate reservoir development. Petroleum 1, 206-216. https://doi.org/10.1016/j.petlm.2015.06.002

Liu, R., Yu, L., Jiang, Y. 2016. Fractal analysis of directional permeability of gas shale fracture networks: A numerical study. Journal of Natural Gas Science and Engineering 33, 1330-1341. https://doi.org/10.1016/j.jngse.2016.05.043

Márquez, M., Jurado, M.J., 2011. Petrophysical characterization of a CO2 storage reservoir using well logs. Geophysical Research Abstracts, vol. 13, EGU2011-6891-3. EGU General Assembly.

Miao, T., M., Yu, B., Duan, Y., Fang, Q. 2015. A fractal analysis of permeability for fractured rocks. International Journal of heat and mass transfer. https://doi.org/10.1016/j.ijheatmasstransfer.2014.10.010

Middleton R. S., Carey, J. W., Currier, R.P., Hyman, J.D., Kang, Q., Karra, S., Jiménez-Martínez, J., Porter M. L., Viswanathan, H. S. 2015. Shale gas and non-aqueous fracturing fluids: Opportunities and challenges for supercritical CO2. Applied Energy, 147, 500-509. https://doi.org/10.1016/j.apenergy.2015.03.023

Mitiku, A.B., Bauer, D.L.S., Beyer, C., 2013. Geochemical modeling of CO2-water-rock interactions in a potential storage formations of the North German sedimentary basin. Applied Geometry 36, 68-186. https://doi.org/10.1016/j.apgeochem.2013.06.008

Nazridoust, K., Ahmadi, G., Smith, D.H. 2006. A new friction factor correlation for laminar, single-phase flows through rock fractures. Journal Hydrogeology 329, 315-328. https://doi.org/10.1016/j.jhydrol.2006.02.032

Ogaya, X., Ledo, J., Queralt, P., Marcuello, A. 2013. First geoelectrical image of the subsurface of the Hontomín site (spain) for CO2geological storage: A magnetotelluric 2D characterization. Int. J. Greenhosue Gas Control 13, 168-179.

Othman, F., Wang, Y. & Hussain, F. 2018a. The Effect of Fines Migration During CO2 Injection Using Pore Scale Characterization. SPE Asia Pacific Oil and Gas Conference and Exhibition. Brisbane, Australia: Society of Petroleum Engineers. https://doi.org/10.2118/192076-MS

Othman, F., Yu, M., Kamali, F. & Hussain, F. 2018b. Fines migration during supercritical CO2 injection in sandstone. Journal of Natural Gas Science and Engineering, 56, 344-357. https://doi.org/10.1016/j.jngse.2018.06.001

Park, Y-Ch., Kim, S., Lee, Y.H., Shinn, Y.J. 2019. Effect of reducing irreducible water saturation in a near-well region on CO2 injectivity and storage capacity. International Journal of Greenhouse Gas Control 86, 134-145. https://doi.org/10.1016/j.ijggc.2019.04.014

Patil, S., Tawfiq, K., Chen, G., 2011. Colloid release and transport in agricultural soil as impacted by solution chemistry. J. Urban Environ. Eng. 5 (2), 84-90. https://doi.org/10.4090/juee.2011.v5n2.084090

Peysson, Y., André, L., Azaroual, M., 2014. Well injectivity during CO2 storage operations in deep saline aquifers- Part 1: Experimental investigation of drying effects, salt precipitation and capillary forces. Int. J. Greenh. Gas Control 22, 291-300. https://doi.org/10.1016/j.ijggc.2013.10.031

Phuc Vu, H., Black, .R, Haese, R.R., 2018. The geochemical effects of O2 and SO2 as CO2 impurities on fluid-rock reactions in a CO2 storage reservoir. Int. J. Greenh. Gas Control 68, 86-98. https://doi.org/10.1016/j.ijggc.2017.11.001

Picot-Colbeaux, G., Pettenati, M., Thiéry, D., Kervévan, Ch., André, L., Azaroual, M., 2009. Numerical modeling of fluid-rock chemical interactions during CO2 saturated water injection into sandstone reservoir, using the MARTHE-REACT code. Proceedings TOUGH Symposium, Lawrence Berkeley National Laboratory, Berkeley, California, September 14-16.
https://hal-brgm.archives-ouvertes.fr/hal-01073955

Pokrovsky, O. S., Golubev, S.V., Schott, J., 2005. Dissolution kinetics of calcite, dolomite and magnesite at 25ºC and 0 to 50 atm ρCO2, Chem. Geol. 217 (3-4), 239-255.
https://doi.org/10.1016/j.chemgeo.2004.12.012

Portier, S., André, L., Vuataz, F-D. 2007. Review on chemical stimulation techniques in oil Industry and applications to geothermal systems. Technical Report. CREGE - Centre for Geothermal Research, Neuchâtel, Switzerland.

Prommer, H., et al., 2013. Final Report - Aquifer Storage and Recovery of Potable Water in the Leederville Aquifer. CSIRO Water for a Healthy Country National Research Flagship, Australia.

Quesada, S., Robles, S., Rosales, I. 2005. Depositional architecture and transgressive-regressive cycles within Liassic backstepping carbonate ramps in the Basque-Cantabrian basin, northern Spain. J. Geol. Soc. 162, 531-538.

Rabbani, E., Davarpanah, A., Memariani, M. 2018. An experimental study of acidizing operation performances on the wellbore productivity index enhancement. J Pet Explor Prod Technol. https://doi.org/10.1007/s13202-018-0441-8

Rosenbauer, R. J., Koksalan, T. 2002. GSA Abstracts with Programs, Annual Meeting, Denver, CO, vol. 135 (2), p. 304.

Rosenbauer, R. J., Koksalan, T., Palandri, L., 2005. Experimental investigation of CO2-brine-rock interactions at elevated temperature and pressure: Implications for CO2 sequestration in deep-saline aquifers, Fuel Process. Technol. 86 (14-15), 1581-1597.
https://doi.org/10.1016/j.furpoc.2005.01.011

Rubio, F.M., García, J., Ayala, C., Rey, C., García Lobón, J.L., 2014. Gravimetric characterization of the geological structure of Hontomin. 8ª Asamblea Hispano-Lusa de Geodesia y Geofísica, Évora (Portugal), 29-31 Jannuary 2014.

Russell, T., Pham, D., Neishaboor. M.T., Badalyan, A., Behr, A., Genolet, L., Kowollik, P., Zeinijahromi, A., Bedrikovetsky, P. 2017. Effects of Kaolinite in rocks on fines migration. Journal of natural Gas Science and Engineering 45, 243-255.
https://doi.org/10.1016/j.jngse.2017.05.020

Russell, T., Wong, K., Zeinijahromi, A., Bedrikovetsky, P. 2018. Effects of delayed particle detachment on injectivity decline due to fines migration. Journal of Hydrology 564, 1099-1109.
https://doi.org/10.1016/j.jhydrol.2018.07.067

Schön, J. H., 2015. Physical Properties of Rocks. Fundamentals and Principles of Petrophysics. Vol 65, 2-497, 2nd edition. Elsevier B.V. ISBN: 978-0-08-100404-3; ISSN: 0376-7361.

Shen, C., Bradford, S.A., Li, T., Li, B., Huang, Y., 2018. Can nanoscale surface charge heterogeneity really explain colloid detachment from primary minima upon reduction of solution ionic strength? J. Nanopart Res. 20 (6).
https://doi.org/10.1007/s11051-018-4265-8

Shi, Y., Wang, Ch. 1986. Pore pressure generation in sedimentary basins: Overloading versus aquathermal. Journal of Geophysical Research Atmospheres 91(B2):2153-2162. https://doi.org/10.1029/JB091iB02p02153.

Soong, Y., Goodman, A.L., McCathy-Jones, J.R., 2004. Experimental and simulation studies on mineral trapping of CO2 with brine. Energy Conversion Management 45, 1845-1859. https://doi.org/10.1016/j.enconman.2003.09.029

Soulaine, C. On the origin of Darcy´s Law. Chapter 1. 2015. https://web.stanford.edu/~csoulain/PORE_SCALE/Chap1_Darcy.pdf Csoulain@stanford.edu
Takenouchi, S., Kennedy, G.C. 1964. Am. J. Sci. 262, 1055 -1074.

Tavani, S. 2012. Plate kinematics in the Cantabrian domain of the Pyrenean orogen. Solid Earth 3, 265-292.

Valle, L.M., Martínez, C., 2015. Patente Nacional: Equipo para ensayos petrofísicos. P201231913.2015.

Valle L.M., Rodríguez R., Grima C., Martínez C., 2018. Effects of supercritical CO2 injection on sandstone wettability and capillary trapping. Int. J. Greenh. Gas Control 78, 341-348. https://doi.org/10.1016/j.ijggc.2018.09.005

Van Golf-Racht, T.D. 1982.Chapter 4: Physical properties of rocks. Developments of fractured reservoir engineering. Volume 12. Fundamentals of fractured reservoir engineering, Pages 147-253. https://doi.org/10.1016/S0376-7361(08)70338-8

Wang, F.P., Reed, R.M., 4e7 October 2009. Pore networks and fluid flow in gas shales. In: SPE Annual Technical Conference and Exhibition. New Orleans, Louisiana, USA.

Wang, L., Yao, B., Xie, H., Winterfeld, P. H., Kneafsey, T. J., Yin, X., Wu, Y. 2017. CO2 injection-induced fracturing in naturally fractured shale rocks. Energy 139, 1094-1110.

Wang, Y., Crandall, D., Bruner K, Ning W., Gill, M., Xiaochun, L., Bromhal, G., 2013. Core and pore scale characterization of Liujiagou Outcrop sandstone, Ordos basin, China for CO2 Aquifer Storage. Energy Procedia 37, 5055-5062. https://doi.org/10.1016/j.egypro.2013.06.419

Williams, B.B., Nierode, D. E. 1972. Design of acid fracturing treatments. SPE-3720-PA, 24, 07. https://doi.org/10.2118/3720-PA

Yan, Q., Lemanski, C., Karpyn, Z. T., Ayala, L. F. 2015. Experimental investigation of shale gas production impairment due to fracturing fluid migration during shut-in time. Journal of Natural Gas Science and Engineering, 24, 99-105. https://doi.org/10.1016/j.jngse.2015.03.017

Yang, D., Tontiwachwuthikul, P., Gu, Y., 2005. Interfacial Tensions of the Crude Oil + Reservoir Brine + CO2 Systems at Pressures up to 31 MPa and Temperatures of 27°C and 58°C. Journal of Chemical Engineering Data, 50(4), 1242-1249.

Yang, D., Gu, Y., Tontiwachwuthikul, P., 2008. Wettability Determination of the Reservoir Brine−Reservoir Rock Systems with Dissolution of CO2 at High Pressures and Elevated Temperatures. Energy & Fuels, 22(1), 504-509.

Yuan, B., Wood, D.A., Yu, W., 2015. Stimulation and hydraulic fracturing technology in natural gas reservoirs: theory and case studies (2012-2015). J. Nat. Gas Sci. Eng. 26, 1414-1421. https://doi.org/10.1016/j.jngse.2015.09.001

Yue, H., Liu, F., Xue, H., Sang, Y., Zhou, Ch., Wang, Y. 2018. Numerical simulation and field application of diverting acid acidizing in the lower Cambrian Longwangmiao Fm gas reservoirs

in the Sichuan Basin. Natural Gas Industry B (5), 3, 204-211.
https://doi.org/10.1016/j.ngib.2018.04.007

Zeinijahromi, A., Farajzadeh, R., Bruining, J., 2016. Effect of fines migration on Oil-water relative permeability during two-phase flow in porous media. Fuel 176, 222-236. https://doi.org/10.1016/j.fuel.2016.02.066

Zhang, X., Ge, J., Kamali, F., Othman, F., Wang, Y., Le-Hussain, F. 2020. Wettability of sandstone rocks and their mineral components during CO2 injection in aquifers: Implications for fines migration. Journal of Natural gas Science and Engineering, 73, 103050. https://doi.org/10.1016/j.jngse.2019.103050

Zhao, L., Pan, Y., Liu, Y., Meng, X., Gui, Y., Liu, P. 2018. Research and performance evaluation on an HA integrated acid system for sandstone acidizing. Natural Gas Industry B (5), 2, 156-161. https://doi.org/10.1016/j.ngib.2018.04.002

Zhao, Z., Jing, L., Neretnieks, I., Moreno, L., 2011. Numerical modeling of stress effects on solute transport in fractured rocks. Comput. Geotech. 38 (2), 113-126.

Zheng, X.L., Shan, B.B., Chen, L., Sun, Y.W., Zhang, S.H., 2014. Attachment-detachment dynamics of suspended particle in porous media: experiment and modeling. J. Hydrol. 511, 199-204.
https://doi.org/10.1016/j.jhydrol.2014.01.039